Journal of Turbulence
Vol. 00, No. 00, 2011, 1–21

RESEARCH ARTICLE

Streak instability in near-wall turbulence revisited

Andrea Cassinelli, Matteo de Giovanetti, Yongyun Hwang*

Department of Aeronautics, Imperial College London, South Kensington, London SW7 2AZ, UK;

(*v3.2 released February 2009*)

The regeneration cycle of streaks and streamwise vortices plays a central role in the sustainment of near-wall turbulence. In particular, the streak breakdown phase in the regeneration cycle is the core process in the formation of the streamwise vortices, but its current understanding is limited particularly in a real turbulent environment. This study is aimed at gaining fundamental insight into the underlying physical mechanism of the streak breakdown in the presence of background turbulent fluctuation. We perform a numerical experiment based on direct numerical simulation, in which streaks are artificially generated by a body forcing computed from previous linear theory. Upon increasing the forcing amplitude, the artificially driven streaks are found to generate an intense fluctuation of the wall-normal and spanwise velocities in a fairly large range of amplitudes. This cross-streamwise velocity fluctuation shows its maximum at $\lambda_x^+ \approx 200-300$ (λ_x^+ is the inner-scaled streamwise wavelength), but it only appears for $\lambda_x^+ \lesssim 3000-4000$. Further examination with dynamic mode decomposition reveals that the related flow field is composed of sinuous meandering motion of the driven streaks and alternating cross-streamwise velocity structures, clearly reminiscent of sinuous-mode streak instability found in previous studies. Finally, it is shown that these structures are reasonably well aligned along the critical layer of the secondary instability, indicating that the surrounding turbulence does not significantly modify the inviscid inflectional mechanism of the streak breakdown via streak instability and/or streak transient growth.

Keywords: streak instability, sinuous mode, streamwise vortices, regeneration mechanism

1. Introduction

Since discovery of the near-wall coherent structures in 1960s [1], significant research efforts have been devoted to their precise understanding. Two predominant coherent structures, *streaks* and *streamwise vortices*, have been found in the near-wall region. Streaks [1, 2] are a spanwise alternating pattern of high- and low-momentum streamwise flow, characterised by a spanwise wavelength of $\lambda_z^+ = 100$ and a long streamwise wavelength of $\lambda_x^+ = 1000$. On the other hand, streamwise vortices [3] are characterized by a spanwise spacing of $\lambda_z^+ = 100$, while their streamwise extent is $\lambda_x^+ \approx 200-300$, much shorter than that of the streaks [4]. The interaction between streaks and streamwise vortices has been understood to play a central role in near-wall turbulence production (see also [5] for an early review).

The concept of the 'minimal flow unit' using direct numerical simulation has enabled significant progress in illuminating low-dimensional dynamics of the near-wall structures. Introduced by [6], it is based on the idea of reducing the computational domain while keeping it constrained to have sustaining of turbulence, hence allowing for the flow features only relevant to the near-wall region. Hamilton *et al.* [7] conducted such a numerical experiment for plane Couette flow at a

*Corresponding author. Email: y.hwang@imperial.ac.uk

ISSN: 1468-5248 (online only)

DOI: 10.1080/14685248.YYYYxxxxxx
http://www.tandfonline.com

low Reynolds number and showed the existence of a cyclic regeneration process of near-wall structures. This process, often called the self-sustaining process, was shown to be made up of three distinct phases: formation of streaks via linear lift-up effect from streamwise vortices, streaks breakdown due to instability and, finally, streamwise vortices regeneration via nonlinear mechanisms. Jimenéz & Pinelli [8] further confirmed that this near-wall process is indeed independent of the flow in the logarithmic and outer regions by showing survival of the near-wall motions in the absence of outer turbulence. Using a similar numerical experiment constraining the computational domain only in the spanwise direction, Hwang [9] recently showed that this self-sustaining near-wall turbulence below $y^+ \simeq 50$ statistically remains the same in a range of moderate Reynolds numbers.

There have also been a number of theoretical investigations on the origin of near-wall coherent structures. In particular, the amplification of streaks in the self-sustaining process has been very well understood with the *lift-up effect*, the mechanism by which streamwise vortices transfer energy of the mean shear to streaks [10–16]. The lift-up effect is associated with the non-normality of the linearised Navier-Stokes operator, and it yields large transient growth of streaks in linearly stable flows. It is important to mention that this amplification mechanism of the streaks plays a central role in determining the spanwise spacing of streaks, i.e. $\lambda_z^+ \simeq 100$. For example, introducing constraints relevant to near-wall turbulence in the evolution time scale [13] or in the wall-normal location [14] was shown to provide $\lambda_z^+ \simeq 100$ for the largest amplification of the streaks. More recently, incorporation of an eddy viscosity into the linearised Navier-Stokes equation was shown to predict the amplification with $\lambda_z^+ \simeq 100$ without such constraints, while providing physically more sound predictions for the structures in the logarithmic and outer regions [14–18].

Contrary to the large number of previous work on streak amplification, the physical processes of generation of streamwise vortices from the linearly amplified streaks have been much less studied. It has been believed that nonlinearity plays an important role in these processes. Hamilton *et al.* [7] initially proposed that an instability of the amplified streaks would be the initiating mechanism of new streamwise vortices and that the following nonlinear processes are responsible for their subsequent amplification. Schoppa & Hussain [19] examined an existing channel flow database at the time [3], and estimated that streaks subject to normal-mode secondary instability would be only 20% of the total. They proposed that the initiating mechanism of the streamwise vortices is more likely to be transient growth of perturbations around weaker linearly stable streaks (i.e. streak transient growth) rather than to be the normal-mode instability of streaks. Later, Hœpffner *et al.* [20] computed optimal transient growth of the streaks in laminar boundary layer. They found that a sinuous-type eigenmode is predominant in both normal-mode streak instability and streak transient growth, indicating that the underlying physical mechanism of the two processes is not very different from each other.

While it has been much less understood, another important role, played by the streak instability and/or the streak transient growth, appears to be determination of the streamwise length scale of the near-wall structures. Indeed, the normal-mode stability analysis in [19] shows that the most unstable streamwise wavelength of the conditionally averaged streaks is $\lambda_x^+ \simeq 200 \sim 400$, which well corresponds to the streamwise extent of the near-wall streamwise vortices. Furthermore, the longest streamwise wavelength of the instability found in [19] is $\lambda_x^+ \simeq O(1000)$, implying that the excitation of the streamwise vortices at longer length scales that this would not be physically possible. Indeed, the typical streamwise length of the streaks in the near-wall region is $\lambda_x^+ \simeq 1000$, although all the existing predictions

by the aforementioned linear theories have shown that the largest amplification of the streaks appears with infinitely long streamwise wavelength (i.e. $\lambda_x^+ \simeq \infty$). In support of this observation, it is also worth mentioning [21], in which the feeding mechanisms of the streamwise vortices were shown not to be active at $\lambda_x^+ > 1000$.

Despite this fundamental importance of streak instability and streak transient growth in the near-wall turbulence, many of previous studies [7, 19] analysed stability of streaky base flow without considering the role of background turbulence. However, as shown by a number of recent linear analyses for streak amplification via the lift-up effect, incorporation of the effect of turbulence into a stability analysis for turbulent flow may play a critical role in gaining more sound physical insight into the coherent structure dynamics in wall-bounded turbulent shear flows [14–17]. Indeed, the presence of background turbulence may significantly distort the dispersion relation and the corresponding eigenstructure of the streak instability. However, stability analyses of streaks incorporating background turbulence are very rare: only two studies are currently available in literature [22, 23], and they are also for the streaky structures in the logarithmic and outer regions (see also [24] for this issue). Furthermore, in these studies, the effect of background turbulence is simply modelled with a crude eddy viscosity, raising a question of whether or not the eddy viscosity would faithfully represent the effect of background turbulence.

The goal of the present study is to directly address this issue arising in the analysis of streak instability in a turbulent flow. In particular, we aim to fully incorporate the role of background turbulence without using any model. To this end, we introduce a novel numerical experiment based on a set of direct numerical simulations, in which the streaks are artificially driven by a stationary body forcing in the form of pairs of counter-rotating streamwise vortices. We note that this body forcing is directly obtained from one of our previous works [16], and it is designed to drive the largest amplitude of streaks subject to the linearised Navier-Stokes equation with an eddy viscosity. The amplitude of the body forcing is then gradually increased for direct observation of streak instability. With careful observation of the cross-streamwise statistics and the velocity spectra, dynamic mode decomposition (DMD) is employed [25, 26] to explore more detailed information of the streak instability, such as the phase speed and the eigenstructure. A discussion on the present results is then given, and the paper finally concludes with some remarks.

2. Numerical experiment

2.1. *Body forcing*

We consider fluid flow over a plane channel with height $2h$. Density and kinematic viscosity of the fluid are respectively denoted by ρ and ν. The streamwise, wall-normal and spanwise directions are denoted as x, y, and z, respectively. The bottom and top walls are set to be located at $y = 0$ and $y = 2h$, respectively. Using the approach in [16], we compute the body forcing which can drive the streaks for its subsequent use for direct numerical simulations. As in [27], the velocity field $\mathbf{u} = (u, v, w)$ is considered to be decomposed such that:

$$\mathbf{u} = \mathbf{U}_0 + \mathbf{u}' + \tilde{\mathbf{u}}, \tag{1}$$

where $\mathbf{U}_0 = (U_0(y), 0, 0)$ is the mean velocity, $\mathbf{u}'$ the turbulent velocity fluctuation, and $\tilde{\mathbf{u}}$ the organised part of the motions, respectively. If the role of the surrounding turbulent velocity fluctuation $\mathbf{u}'$ in the organised wave $\tilde{\mathbf{u}}$ is approximated with an

eddy-viscosity-based model, the following equation is obtained for small $\tilde{\mathbf{u}}$:

$$\nabla \cdot \tilde{\mathbf{u}} = 0, \tag{2a}$$

$$\frac{\partial \tilde{\mathbf{u}}}{\partial t} + (\nabla \cdot \mathbf{U}_0)\tilde{\mathbf{u}} + (\nabla \cdot \tilde{\mathbf{u}})\mathbf{U}_0 = -\frac{1}{\rho}\nabla \tilde{p} + \nabla \cdot [\nu_T(\nabla \tilde{\mathbf{u}} + \nabla \tilde{\mathbf{u}}^T)] + \tilde{\mathbf{f}}, \tag{2b}$$

where $\tilde{p}$ is the pressure of the small organised wave, and $\tilde{\mathbf{f}} = (\tilde{f}_u, \tilde{f}_v, \tilde{f}_w)$ is the forcing term to be computed.

As in previous studies [14–16], the semi-empirical model proposed by Cess is considered for the total viscosity ν_T:

$$\nu_T(\eta) = \frac{\nu}{2}\Big\{1 + \frac{\kappa^2 Re_\tau^2}{9}(1-\eta^2)^2(1+2\eta^2)^2 \times 1 - e^{[(|\eta|-1)Re_\tau/A]^2}\Big\}^{\frac{1}{2}} + \frac{\nu}{2}. \tag{3}$$

Here, $\eta = (y-1)/h$, $\kappa = 0.426$ and $A = 25.4$ from [14]. Also, $\nu_T = \nu + \nu_t$ where ν_t is the eddy viscosity. The mean-velocity profile $U(y)$ is then obtained by considering Prandtl's mixing length model $\nu_t dU/dy = -\overline{u'v'}$. It should be noted that the use of the eddy viscosity (3) for (2) is an approximation for the role of surrounding turbulence with an assumption that the perturbation would feel surrounding turbulence in the way that the mean velocity does, given the nature of the eddy viscosity directly related to the mean velocity. Therefore, in principle, the eddy viscosity model would perform well at best for the motions, the time scale of which is much larger than or at least is at the order of the time scale of the mean shear (i.e. $O(1/S)$ where $S \sim O(dU_0/dy)$). Despite this inherent limitation, it has been shown that the linear model (2) with the eddy viscosity (3) provides physically sound prediction for coherent structures (especially streaks) at high Reynolds numbers [14–16, 18]. This is essentially because the eddy viscosity properly incorporates inhomogeneous turbulent dissipation in the wall-normal direction, as extensively discussed in a recent work [18].

Since the flow is homogeneous in the two wall-parallel directions, we consider a single plane Fourier mode for $\tilde{\mathbf{u}}$ and $\tilde{\mathbf{f}}$:

$$\tilde{\mathbf{u}} = \hat{\mathbf{u}}(y,t;k_x,k_z)e^{\mathrm{i}(k_x x + k_z z)}, \tag{4a}$$

$$\tilde{\mathbf{f}} = \hat{\mathbf{f}}(y,t;k_x,k_z)e^{\mathrm{i}(k_x x + k_z z)}, \tag{4b}$$

where k_x and k_z are the streamwise and spanwise wavenumbers, respectively. If a harmonic forcing with angular frequency ω_f is exerted on the system for given k_x and k_z (i.e. $\hat{\mathbf{f}}(y,t) = \hat{\mathbf{f}}_\omega(y)e^{\mathrm{i}\omega_f t}$), the response takes the form of $\hat{\mathbf{u}}(y,t) = \hat{\mathbf{u}}_\omega(y)e^{\mathrm{i}\omega_f t}$ for sufficiently large t. This then allows one to pose an optimisation problem to find the forcing $\hat{\mathbf{f}}_\omega$ which induces the largest energy in the system: i.e.

$$\max_{\hat{\mathbf{f}}_0 \neq 0} \frac{||\hat{\mathbf{u}}_\omega||^2}{||\hat{\mathbf{f}}_\omega||^2}, \tag{5}$$

where $||\hat{\mathbf{u}}_\omega||^2 = (1/h)\int_{-h}^{h} \hat{\mathbf{u}}_\omega^H \hat{\mathbf{u}}_\omega \, dy$ (the superscript ^{H} denotes the complex conjugate transpose). The optimisation problem in (5) is solved with the code used in [16]. It is based on a Chebyshev-collocation method for discretizing the Orr-Sommerfeld Squire system in the wall-normal direction [28]. The resulting numerical optimisation problem is solved using the standard method in [29].

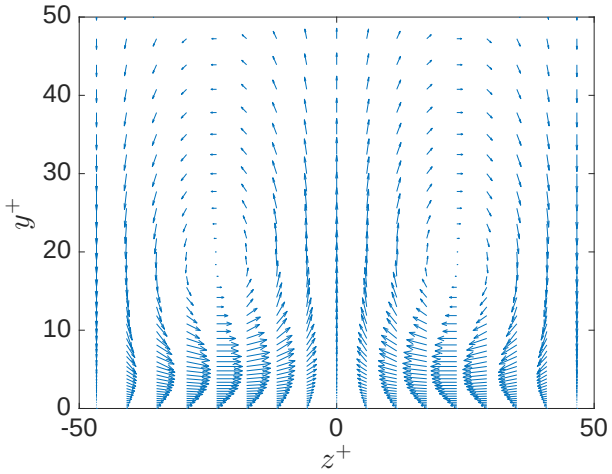

Figure 1. Optimal forcing in the near-wall region. $\lambda_z^+ = 100$, $\lambda_x^+ = \infty$, $\omega_f = 0$ and $Re_\tau = 180$

The body forcing is computed for $\lambda_z^+ = 100$ and $\lambda_x^+ = \infty$ at $Re_\tau = 180$ with $N_y = 129$ (N_y is the number of grid points in the wall-normal direction). Figure 1 reports the computed body forcing (i.e. $\mathbf{f} = \mathrm{Re}[\tilde{\mathbf{f}}(y)e^{ik_z z}]$). The structure of the forcing is clearly given in the form of a pair of counter-rotating streamwise vortices concentrated in the near-wall region ($y^+ < 60$), consistent with [16]. Here, we note that this body forcing does not necessarily generate the largest possible amplification of streaks in a real turbulent flow, as it is obtained with a crude eddy viscosity. However, we should also point out that it is difficult to avoid a certain level of artificiality in the design of such a body forcing, as there is no systematic way to design a body forcing that generates exactly the same streaks as those in real flows. In this respect, the use of the present linear model is essentially to minimise such artificiality based on our previous studies [e.g. 16], which have robustly shown that the body forcing from the linear model (2) can generate streaks fairly similar to those in the near-wall region. Indeed, what is the most crucial is the counter-rotating streamwise vortical form of the body forcing in the near-wall region. Such form of artificial body forcing has also been previously used in [30] where a set of invariant solutions of Couette flow are computed using continuation with the streak instability mode.

2.2. *Direct numerical simulation*

The computed body forcing is subsequently implemented to a direct numerical simulation. The direct numerical simulation code employed here is `diablo` [31], and it has been validated in previous studies [e.g. 9]. The x- and z-directions are discretised using the Fourier-Galerkin method with the 2/3 rule for dealiasing, while the wall-normal direction is discretised using second-order central differences. The time integration is performed semi-implicitly using the fractional-step method [32]. All terms with y-derivatives are implicitly advanced with second-order Crank-Nicolson method, while the rest of the terms are explicitly integrated using a third order low-storage Runge-Kutta method. All the computations are performed by imposing a constant mass flux across the channel.

The computational domain for the present numerical experiment is chosen to be $L_x \times L_y \times L_z = 6\pi h \times 2h \times \pi h$. The relatively long streamwise domain is chosen to allow for a range of streamwise wavelengths of streak instability. The Reynolds number based on the bulk velocity U_b is chosen as $Re_b (\equiv 2U_b h/\nu) = 5600$. The

reference simulation without the body forcing yields the friction Reynolds number $Re_\tau \simeq 180$. The number of grid points are set to be $N_x \times N_y \times N_z = 288 \times 129 \times 96$ (after dealiasing). This gives $\Delta_x^+ = 11.8$ and $\Delta_z^+ = 5.9$, which are slightly finer than those in [3]. The wall-normal direction is appropriately stretched to provide a fine resolution in the near-wall region.

The body forcing obtained from the linear theory (figure 1) is implemented to the direct numerical simulation. The spanwise computational domain considered (${L_z}^+ \simeq 565$) allows us to implement the body forcing composed of six pairs of counter-rotating streamwise vortices with the spanwise spacing of $\lambda_z^+ \approx 94$. All the cross-streamwise statistics in section 3 are obtained by averaging them for $T = 30h/u_\tau$ where u_τ is the friction velocity of the reference simulation. Throughout the present study, all the data are scaled with the friction velocity of the reference simulation u_τ to assess the effect of the forcing.

2.3. *Dynamic mode decomposition*

The eigenstructure of the streak instability is detected by performing dynamic mode decomposition (DMD) on the data of direct numerical simulations [25, 26]. The DMD approximates the temporal (or spatial) evolution of given flow fields onto a finite dimensional linear time-invariant (LTI) dynamical system. The LTI system is typically constructed with a series of flow-field snapshots, and it may become an approximation of the Koopman operator especially if the snapshots are obtained with a statistically stationary attractor. The algorithm of DMD in this study follows the one in [25, 26], where the LTI system is projected onto a subspace created by the proper orthogonal decomposition (POD) modes to enhance robustness of DMD. For further details on the DMD algorithm, the reader may refer to [26].

We consider a series of flow-field snapshots equispaced in time with the interval Δt: $\boldsymbol{\psi}_n \equiv \boldsymbol{\psi}(n\Delta t)$, where $\boldsymbol{\psi}_n$ is a flow field (or variable) of interest. Each data snapshot is assumed to contain M complex elements without loss of generality. If we assume that the temporal evolution of the given flow fields is generated by a discrete-time linear time-invariant system, it can be written as

$$\boldsymbol{\psi}_{n+1} = \mathbf{A}\boldsymbol{\psi}_n, \qquad \text{for} \quad n = 0, 1, ..., N-1. \tag{6}$$

Supposing that $N+1$ samples in time are collected, we can form the following two matrices:

$$\boldsymbol{\Psi}_0 = [\boldsymbol{\psi}_0 \ \boldsymbol{\psi}_1 \ \cdots \ \boldsymbol{\psi}_{N-1}] \qquad \in \mathbb{C}^{M\times N}, \tag{7a}$$

$$\boldsymbol{\Psi}_1 = [\boldsymbol{\psi}_1 \ \boldsymbol{\psi}_2 \ \cdots \ \boldsymbol{\psi}_N] \qquad \in \mathbb{C}^{M\times N}. \tag{7b}$$

The relation between $\boldsymbol{\Psi}_0$ and $\boldsymbol{\Psi}_1$ is then given by

$$\boldsymbol{\Psi}_1 = \mathbf{A}\boldsymbol{\Psi}_0. \tag{8}$$

We then project $\mathbf{A}$ onto the space spanned by the POD modes of $\boldsymbol{\Psi}_0$, such that:

$$\mathbf{A} \simeq \mathbf{U}\mathbf{F}\mathbf{U}^H, \tag{9}$$

where $\mathbf{U} \in \mathbb{C}^{M\times r}$ is a unitary matrix, the column vector of which corresponds to each POD mode, and the superscript ^{H} denotes the complex conjugate transpose.

The matrix $\mathbf{U}$ is obtained by an economy-size singular value decomposition (SVD) of $\mathbf{\Psi}_0$:

$$\mathbf{\Psi}_0 = \mathbf{U}\mathbf{\Sigma}\mathbf{V}^H, \tag{10}$$

where $\mathbf{\Sigma} = diag\{\sigma_1, \sigma_2, ..., \sigma_r\}$ with non-zero singular value σ_n for $n = 1, 2, .., r$, and $\mathbf{V} \in \mathbb{C}^{r\times N}$ is a unitary matrix, the row vector of which characterises the temporal dynamics of each POD mode. Finally, minimisation of the difference between the left-hand and the right-hand sides in (8) gives

$$\mathbf{F} = \mathbf{U}^H\mathbf{\Psi}_1\mathbf{V}\mathbf{\Sigma}^{-1}, \tag{11}$$

where $\mathbf{F} \in \mathbb{C}^{r\times r}$.

Now, we assume that $\mathbf{F}$ has linearly independent eigenvectors $\mathbf{y}_j$ and the corresponding eigenvalues μ_j for $j = 1, 2, ..., r$. Then, $\mathbf{U}\mathbf{y}_j$ and μ_j respectively approximate the eigenvectors and eigenvalues of $\mathbf{A}$ (DMD modes). Using the eigenfunction expansion, the evolution of a given flow field is approximated by

$$\boldsymbol{\psi}_n \approx \sum_{j=1}^{r} \alpha_j \mu_j^n \mathbf{U}\mathbf{y}_j, \tag{12}$$

where α_j represents as the 'amplitude' of the corresponding DMD modes. In the present study, α_j has been computed following the optimisation procedure given in [26].

3. Results and discussion

3.1. *Streak amplification*

As described in section 2.2, a set of direct numerical simulations are performed with the real part of the stationary optimal body forcing computed in section 2.1 (figure 1). To be consistent with the definition of the norm in (5), the forcing amplitude is defined such that:

$$\|\mathbf{f}\| = \frac{2}{V}\int_V \mathbf{f}^H\mathbf{f}\,dV, \tag{13}$$

where $V(= L_x \times L_y \times L_z)$ is the volume of the computational domain. A relatively wide range of the forcing amplitude is considered from $\|\mathbf{f}\| = 0$ to $\|\mathbf{f}\| = 4.7\,u_\tau^2/h$. Application of the body forcing with sufficiently large forcing amplitudes has been found to yield non-negligible elevation of turbulent skin friction. We note that this is somehow expected, as the 'lift-up' effect has recently been found to play a crucial role in turbulent skin-friction generation by mediating the streamwise momentum exchange in the wall-normal direction [33, 34]. The friction Reynolds number of the simulations is therefore found to increase with the forcing amplitude: for example, $Re_\tau = 190$ for $\|\mathbf{f}\| = 0.47\,{u_\tau}^2/h$, $Re_\tau = 202$ for $\|\mathbf{f}\| = 0.94\,{u_\tau}^2/h$, and $Re_\tau = 235$ for $\|\mathbf{f}\| = 2.8\,{u_\tau}^2/h$, respectively.

Figure 2 reports instantaneous flow fields of the streamwise velocity fluctuation, as the forcing amplitude is gradually increased. The flow fields clearly reveal that the considered body forcing generates the streaky structure extending over the entire streamwise domain. More careful inspection also enables us to observe that the artificially driven streaks actually meander in the streamwise direction (see e.g.

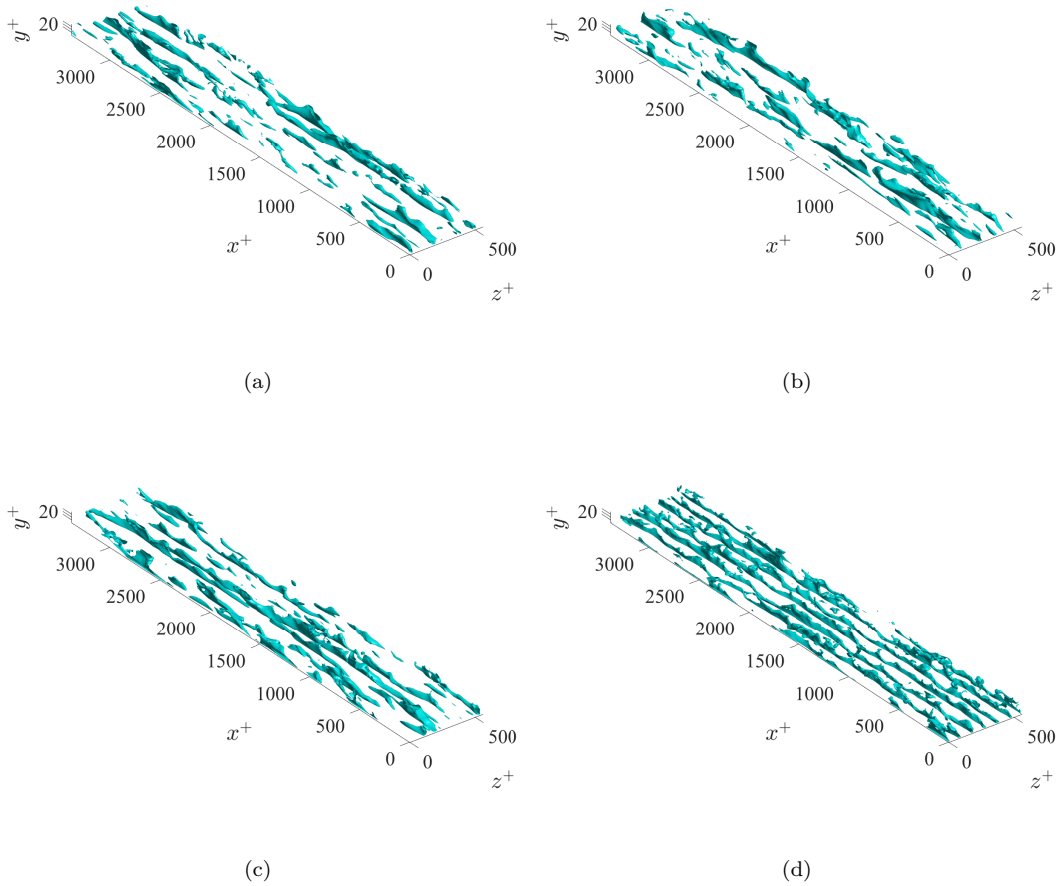

Figure 2. Instantaneous field of the streamwise velocity fluctuation ($u'^+ = -4$): (a) $\|\mathbf{f}\| = 0$; (b) $\|\mathbf{f}\| = 0.0470\ u_\tau^2/h$; (c) $\|\mathbf{f}\| = 0.470\ u_\tau^2/h$; (d) $\|\mathbf{f}\| = 4.70\ u_\tau^2/h$.

figure 2*d*). This issue will be discussed in detail with the velocity spectra and the dynamic mode decomposition (see sections 3.2 and 3.3).

Cross-streamwise view of the mean streamwise velocity $U^+(y,z)$ is calculated with the artificially driven streaks, as shown in figure 3. The mean streamwise velocity reveals the action driven by the body forcing in the form of the counter-rotating vortices (figure 1): the low-speed fluid along $z^+ = 0$ is pumped away from the wall, while the high-speed fluid along $z^+ \simeq \pm 50$ is brought to the near-wall region (i.e. lift-up effect). As the forcing amplitude is increased, the formation of the streaks becomes evident in the the mean streamwise velocity $U^+(y,z)$. Especially, the spanwise width of the low-speed region around $z = 0$ appears to be narrower with the increase of the forcing amplitude, whereas that of the high-speed region around $z^+ \simeq \pm 50$ becomes wider. We note that this feature has also been observed from the streaks in transitional boundary layer [35], suggesting that it is probably a general nonlinear behaviour for the high-amplitude streaky flow.

Two statistical measures are introduced to quantify the amplification of the streaks by the body forcing. First, following the triple decomposition introduced in (1) (see also [27]), the norm of the organised part of the streaky turbulent flow is computed, such that:

$$\|\tilde{\mathbf{u}}\| = \|\mathbf{U}(y,z) - \mathbf{U}_0(y)\|, \tag{14}$$

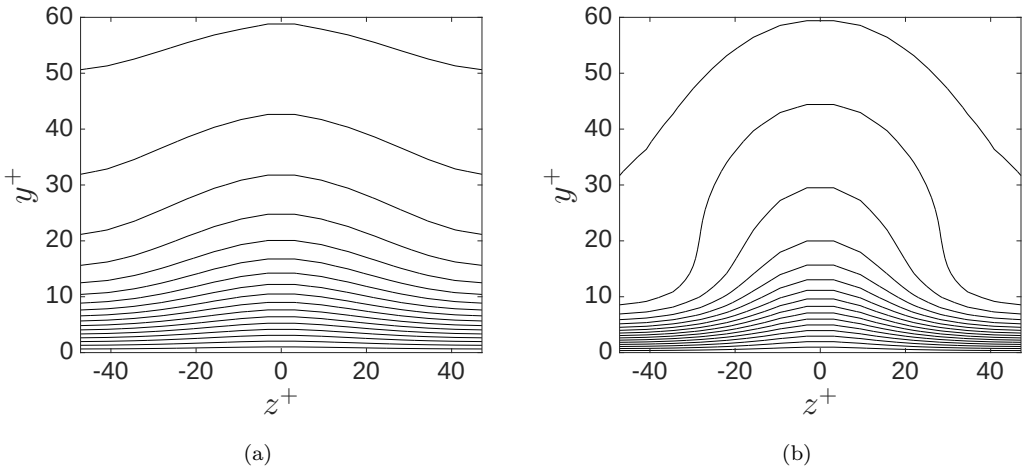

Figure 3. Cross-streamwise view of streaky mean flow $U^+(y,z)$: (a) $\|\mathbf{f}\| = 0.47u_\tau^2/h$ ($A_s^+ = 1.39$); (b) $\|\mathbf{f}\| = 2.82u_\tau^2/h$ ($A_s^+ = 3.24$). Here, the contour labels are uniformly spaced with $\Delta U^+(y,z) = 0.9$.

where $\mathbf{U}(y,z) = (U(y,z), V(y,z), W(y,z))$ is the streaky mean flow obtained with the non-zero body forcing, and $\mathbf{U}_0(y) = (U_0(y), 0, 0)$ is the mean flow without forcing. We note that if the closure model in (2) was correct, $\tilde{\mathbf{u}}$ in (14) for small forcing amplitude would be identical to that in (2). However, this is not likely to happen, given the crudeness of the closure model based on an eddy viscosity in (2). Nevertheless, the computation of $\|\tilde{\mathbf{u}}\|$ with (14) allows us to assess the fidelity of the eddy viscosity model in (2) at least in a partial manner.

The second measure is introduced following the definition of the streak amplitude used in a laminar boundary layer and previous studies [22, 23, 35]. Using the mean velocity, the streak amplitude is defined as:

$$A_s^+ = \frac{1}{2}[\max_{y,z}(U^+(y,z) - U_0^+(y)) - \min_{y,z}(U^+(y,z) - U_0^+(y))]. \tag{15}$$

However, it should be noted that the definition of A_s^+ in (15) is not exactly the same as the one in the previous studies, as $U^+(y,z)$ in (15) is affected by the presence of the streak instability in the flow field especially with the high forcing amplitude. Therefore, care should be taken in interpreting the present results using A_s^+.

Finally, it needs to be mentioned that we have attempted to use the definition based on the streak lift angle for the streak amplitude following [19]. However, application of this definition was found not to suit very well to the streaky mean flows in the present study. While we do not clearly understand the origin of this technical issue, we note that the streaky mean flow in the present study is statistically stationary, as it is driven by a stationary body forcing. However, the one in [19] was obtained with a phase average of the spatio-temporally evolving streaks. Furthermore, although the body forcing obtained in section 2.1 appears to well generate streaky flows in the near-wall region, these streaks would not necessarily be exactly the same as those naturally emerging in the near-wall region. These issues are probably associated with the non-suitability of the streak-lift-angle-based definition in [19] to the present streaky flows. In this respect, it is finally worth mentioning the recent work of [36], in which a new definition on the streak amplitude is introduced. However, in the present study, we have not examined this definition of the streak amplitude.

The two measures for the size of the streaks in (14) and (15) are reported in figure

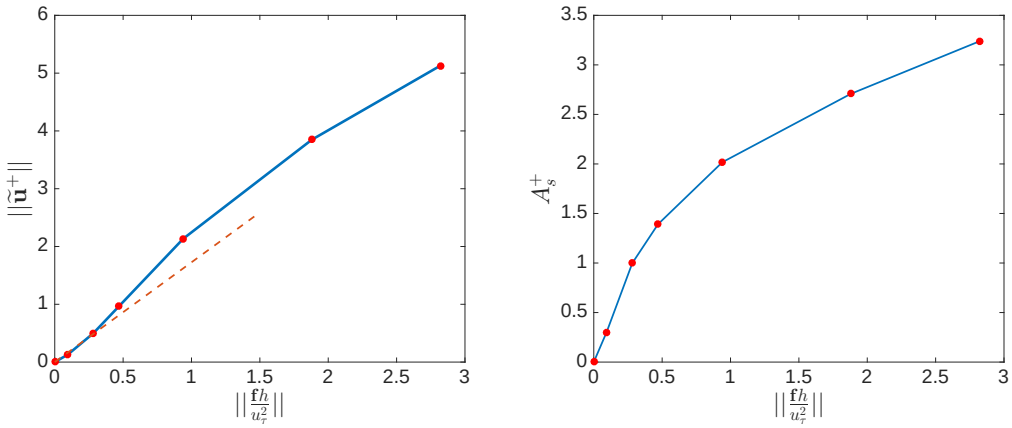

(a) (b)

Figure 4. Flow field response with respect to the forcing amplitude: (*a*) $\|\tilde{\mathbf{u}}^+\|$; (*b*) A_s^+. In (*a*), the linear curve is $\|\tilde{\mathbf{u}}^+\| = 1.73\,\|\mathbf{f}h/u_\tau^2\|$ and is the best fit obtained with the first three points (including zeros).

3.1. As the forcing amplitude $\|\mathbf{f}\|$ is gradually increased, both $\|\tilde{\mathbf{u}}\|$ and A_s^+ are also found to increase. For $\|\mathbf{f}\| \lesssim 0.3u_\tau^2/h$, they roughly appear to increase linearly with $\|\mathbf{f}\|$, although very precise calculation of $\|\mathbf{u}\|$ and A_s^+ for such low amplitudes was found to be fairly difficult due to the statistical error originating from the finite interval for time average. At such small forcing amplitudes, the streak amplification approximately follows a linear fit $\|\tilde{\mathbf{u}}^+\|/\|\mathbf{f}h/u_\tau^2\| \simeq 1.73$. We note that this value is larger than $\|\tilde{\mathbf{u}}^+\|/\|\mathbf{f}h/u_\tau^2\| \simeq 0.85$ obtained by solving the optimisation problem (5) with (2), indicating that the turbulent dissipation provided by the eddy viscosity in (2) appears to be stronger than that by real turbulence. Nevertheless, the value of $\|\tilde{\mathbf{u}}^+\|/\|\mathbf{f}h/u_\tau^2\|$ from the present numerical experiment is still at the same order as that from the linear model (2), indicating that the linear model (2) with the eddy viscosity is not so inaccurate in predicting the streak amplification at least for the forcing profile considered in the present study. This is in sharp contrast to the linear model without eddy viscosity, as it was recently found that exclusion of the eddy viscosity in (2) typically predicts two orders of magnitude larger $\|\tilde{\mathbf{u}}^+\|/\|\mathbf{f}h/u_\tau^2\|$ at this Reynolds number ($Re_\tau \simeq 180$) [37].

3.2. *Statistical evidence of streak instability*

To seek statistical evidence of streak instability, the velocity spectra from the unforced and forced simulations are examined. Figure 5 shows a structural comparison between one-dimensional streamwise wavenumber spectra in the unforced and forced cases. The spectra of the unforced case show the typical features of the near-wall turbulence: the peak at $y^+ \simeq 10-15$ and $\lambda_x^+ \simeq 1000$ in the streamwise wavenumber spectra of streamwise velocity well represents the wall-normal structure and the streamwise length of the near-wall streaks (figure 5*a*), while the peaks at $y^+ \approx 45-50$ and $\lambda_x^+ = 200 \sim 300$ in the spectra of wall-normal and spanwise velocities (figures 5*c*,*e*) well depict the streamwise vortices. Interestingly, introduction of the body forcing at $k_x = 0$ ($\lambda_x^+ \simeq \infty$) does not appear to change these peak locations (note that direct effect of the body forcing is not visible with the logarithmic axis of λ_x^+ in figure 5, as the body forcing is given at $\lambda_x^+ \simeq \infty$): the streamwise velocity spectra still retain the peak at $y^+ \simeq 10-15$ and $\lambda_x^+ \simeq 1000$ (figure 5*b*), and the spectra of wall-normal and spanwise velocities show the peak at $y^+ \approx 45-50$ and $\lambda_x^+ = 200 \sim 300$ (figures 5*d*,*f*). However, the intensities of the

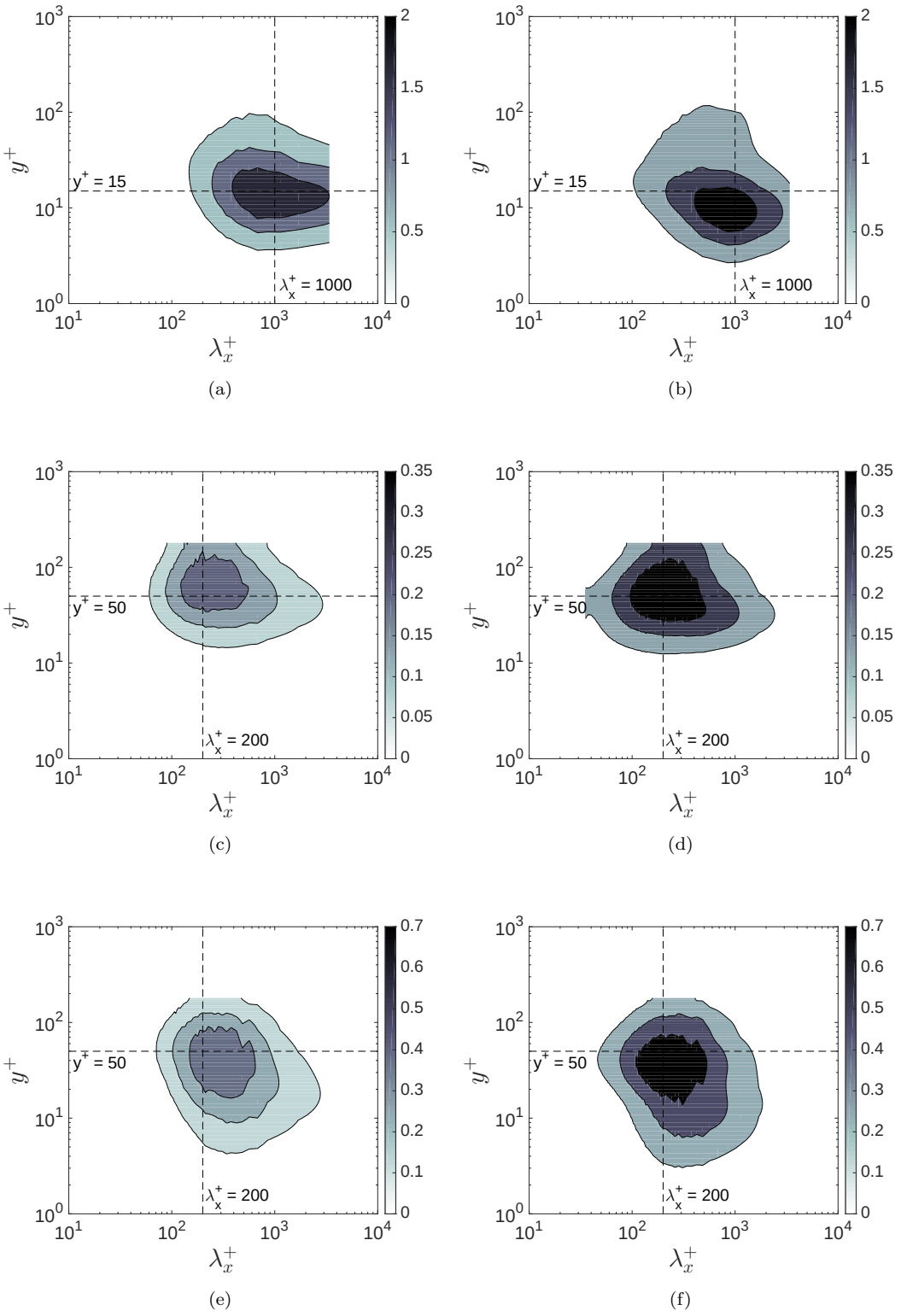

Figure 5. Premultiplied one-dimensional streamwise wavenumber spectra of (a,b) streamwise, (c,d) wall-normal, and (e,f) spanwise velocities: (a, c, e) $\|\mathbf{f}\| = 0$; (b, d, f) $\|\mathbf{f}\| = 2.82u_\tau^2/h$. Here, the contour colour indicates spectral intensity, and the labels indicate 0.25, 0.5, and 0.75 times of the maximum of each spectrum.

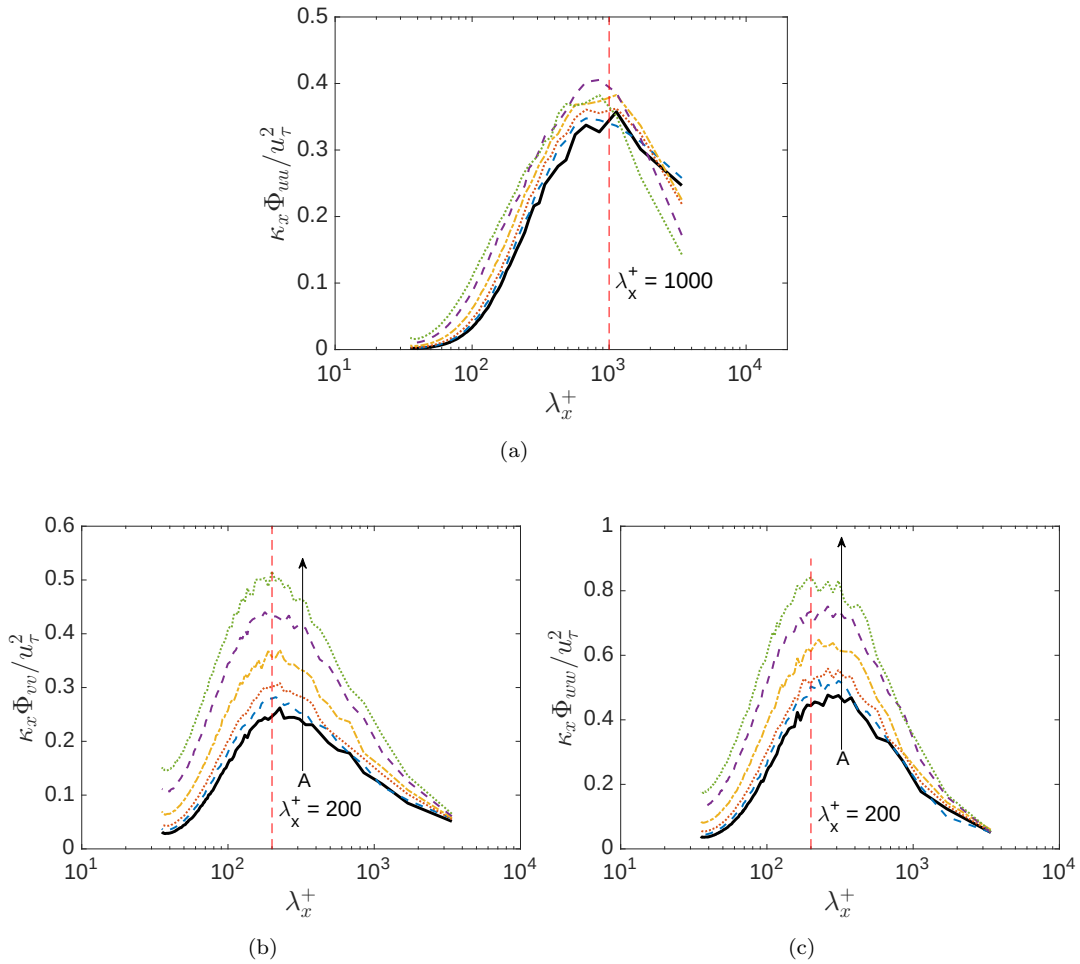

Figure 6. Premultiplied streamwise wavenumber spectra of (*a*) streamwise, (*b*) wall-normal, and (*c*) spanwise velocities. Here, the spectra are taken at their peak wall-normal location shown in figure 5: i.e. $y^+ \approx 15$ for the streamwise velocity, whereas $y^+ \approx 50$ for the wall-normal and spanwise velocities. The curves are: ——, unforced; - - - -, $\|\mathbf{f}\| = 0.282u_\tau^2/h$; ·····, $\|\mathbf{f}\| = 0.470u_\tau^2/h$; – · – · –, $\|\mathbf{f}\| = 0.940u_\tau^2/h$; - - - -, $\|\mathbf{f}\| = 1.880u_\tau^2/h$; ·····, $\|\mathbf{f}\| = 2.820u_\tau^2/h$.

spectra are found to be significantly changed by the body forcing especially for the wall-normal and spanwise velocities (figures 5*d*,*f*), even though the body forcing is given only for zero streamwise wavenumber (see the contour colours of figure 5).

Figure 6 shows how the spectral intensities of each velocity component change on increasing the forcing (or streak) amplitude. The amplification for finite wavelengths $\lambda_x^+ < \infty$ appears only in the wall-normal and spanwise velocity spectra (figures 6*b*,*c*), whereas the streamwise velocity spectra remain roughly the same (figure 6*a*). The largest amplification in the wall-normal and spanwise velocity spectra takes place around $\lambda_x^+ \approx 200 - 300$, and the elevation of the spectral intensity appears to be limited around $\lambda_x^+ \approx 2000 - 3000$ (figures 6*b*,*c*). It should be stressed that the body forcing here is provided only at $\lambda_x^+ = \infty$ and that its main role is to generate the streamwise uniform streaks carrying large streamwise velocity. However, the intensive energy amplification in the spectra of the wall-normal and spanwise velocities at much shorter streamwise wavelengths ($\lambda_x^+ \approx 200 - 300$) clearly suggests that there must be another mechanism in play in addition to the streak amplification. In this respect, it is important to highlight that the short streamwise wavelength of the energy elevation in the spectra ($\lambda_x^+ \approx 200 - 300$) corresponds well to the most unstable streamwise wavelength in the previous streak instability analysis with the molecular viscosity [19]. Furthermore, in their anal-

ysis, the streamwise wavelength of the instability was found to be bounded by $\lambda_x^+ \approx 3000 - 4000$. The energy elevation in the spectra of the cross-streamwise velocity components in our numerical experiment appears to well capture these features, suggesting that the streaks driven by the body forcing in the present numerical experiment are likely to experience the streak instability.

3.3. *Dynamic mode decomposition*

Now, we apply DMD to the numerical simulations to identify the eigenstructure associated with the streak instability. The following data for $y^+ \leq 70$ are taken as the complex snapshots $\boldsymbol{\psi}_n$ in section 2.3:

$$\boldsymbol{\psi}_n(y,z;k_x) = \begin{pmatrix} \hat{u}(y;k_x,k_z)e^{\mathrm{i}k_z z} + \hat{u}(y;k_x,-k_z)e^{-\mathrm{i}k_z z} \\ \hat{v}(y;k_x,k_z)e^{\mathrm{i}k_z z} + \hat{v}(y;k_x,-k_z)e^{-\mathrm{i}k_z z} \\ \hat{w}(y;k_x,k_z)e^{\mathrm{i}k_z z} + \hat{w}(y;k_x,-k_z)e^{-\mathrm{i}k_z z} \end{pmatrix}, \tag{16}$$

where $\hat{u}(y;k_x,k_z)$, $\hat{v}(y;k_x,k_z)$, and $\hat{w}(y;k_x,k_z)$ are respectively the Fourier coefficients of the streamwise, wall-normal and spanwise velocities from DNS. Since the spanwise spacing of the eigenstructure of the streak instability should broadly correspond to the separation of the driven streaks, k_z is given to be the same as that of the body forcing (i.e. $\lambda_z^+ = 94$). The streamwise wavenumber k_x is then chosen in the range of $\lambda_x^+ = 200 - 300$. Once the DMD modes are computed with the eigenvalues μ_j for given k_x and k_z, the associated angular frequency ω_j is computed with $\omega_j = \mathrm{i}\ln\mu_j/(\Delta t)$. The phase speed (i.e. downstream propagating speed) of the DMD mode is then determined as

$$c_j = \frac{\mathrm{i}\ln\mu_j}{k_x \Delta t}, \tag{17}$$

where c_j is the phase speed of the j-th DMD mode. The relative amplitude (or energy) α_j of all the DMD modes is finally determined. The time interval, the number of POD modes, and the number of the snapshots for the DMD in the present study have been carefully chosen to ensure good resolution of the near-wall dynamics: $\Delta t^+ = 0.77$, $r = 30$ and $N = 2000$. A detailed discussion on the choice of these parameters is given in Appendix A.

Figure 7 shows the DMD result for $\lambda_x^+ = 200$. All the computed eigenvalues of the DMD modes μ_j are found to be located over the unit circle in the Re(μ)-Im(μ) plane, indicating that they are almost neutrally stable (figure 7*a*). We note that this is expected, as the applied snapshots are from statistically stationary flow fields. Computation of the phase speed c_j and the amplitude α_j of the DMD modes reveals that their phase speed is consistently observed around $c^+ \simeq 8 - 16$ (figure 7*b*) and, in particular, the most energetic DMD mode shows $c^+ \simeq 11.8$. The phase speed of the most energetic DMD mode is robustly obtained within $c^+ \simeq 11 - 13$ throughout the present study, as long as the DMD parameters are chosen to ensure good resolution for the near-wall dynamics (i.e. $\Delta t^+ < 1$, $r \geq 30$, $N \geq 1000$). We also note that this phase speed is in good agreement with the propagation velocity $c^+ \simeq 10$ of the near-wall structure found in [38].

The structure of the DMD modes is also examined. A typical example of the most energetic DMD mode (the most energetic mode for $N = 2000$, $r = 30$, $\lambda_x^+ = 200$) is visualised in figure 8. The flow structure is characterised by sinuous meandering motion of a streak mainly located for $y^+ \leq 20$ (blue isosurface in figure 8). The structure of the negative wall-normal velocity shows a streamwise-alternating

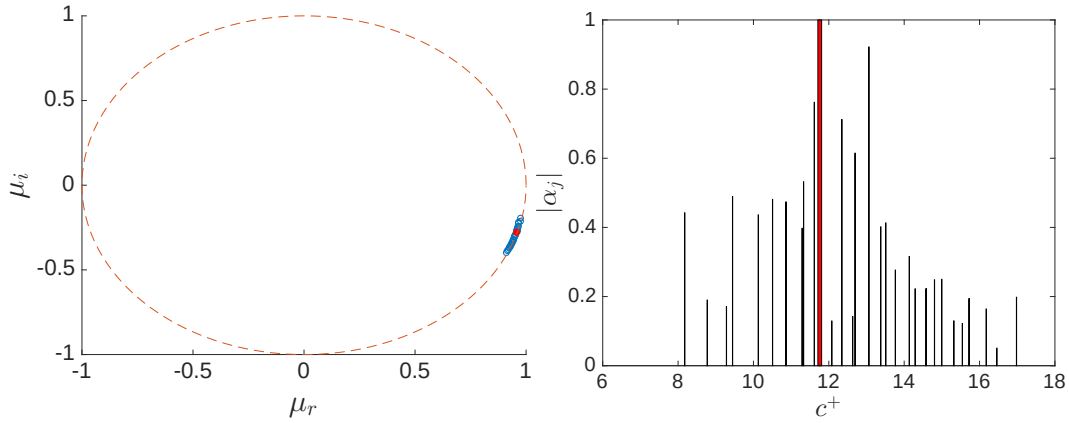

Figure 7. Dynamic mode decomposition ($r = 30$, $N = 2000$, $\|\mathbf{f}\| = 2.82u_\tau^2/h$ and $\lambda_x^+ = 200$): (a) eigenvalues of $\mathbf{F}$, μ_j; (b) the normalised amplitude of the DMD mode, α_j. Here, the red dot and bar indicate the most energetic DMD mode.

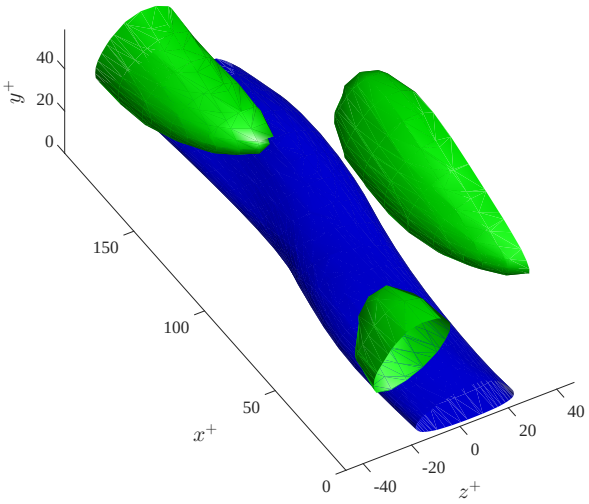

Figure 8. Visualisation of the most energetic DMD mode ($N = 2000$, $r = 30$, $\lambda_x^+ = 200$). To highlight meandering of the low-speed streak, the visualised flow field is chosen to be $\mathbf{u}_{vis} = \mathbf{U}(y,z) - \langle \mathbf{U}(y,z) \rangle_z + k_s \mathbf{u}_{dmd}$ where $\langle \cdot \rangle_z$ denotes average in z-direction, k_s is an appropriate tuning constant for visualisation, and $\mathbf{u}_{dmd}$ is the DMD mode. Here, blue- and yellow-coloured surfaces indicate iso-surfaces of negative streamwise and wall-normal velocity, respectively.

pattern above the streak flanks, and it is elongated and positively inclined in the streamwise direction. This structure of the wall-normal velocity is mainly located at $20 \leq y^+ \leq 60$, consistent with the spectra of the wall-normal velocity in figure 5 where the largest amplification of the spectral intensity is observed at $y^+ \simeq 50$. The structure of the DMD mode in figure 8 is clearly reminiscent of the 'sinuous' mode of the streak instability. It should be noted that this structure is a robust feature to the choice of the DMD parameters. Indeed, most of the most energetic DMD modes computed by varying the DMD parameters are in this form (i.e. the streamwise wavelength λ_x^+, the number of snapshots N, and the number of POD modes r).

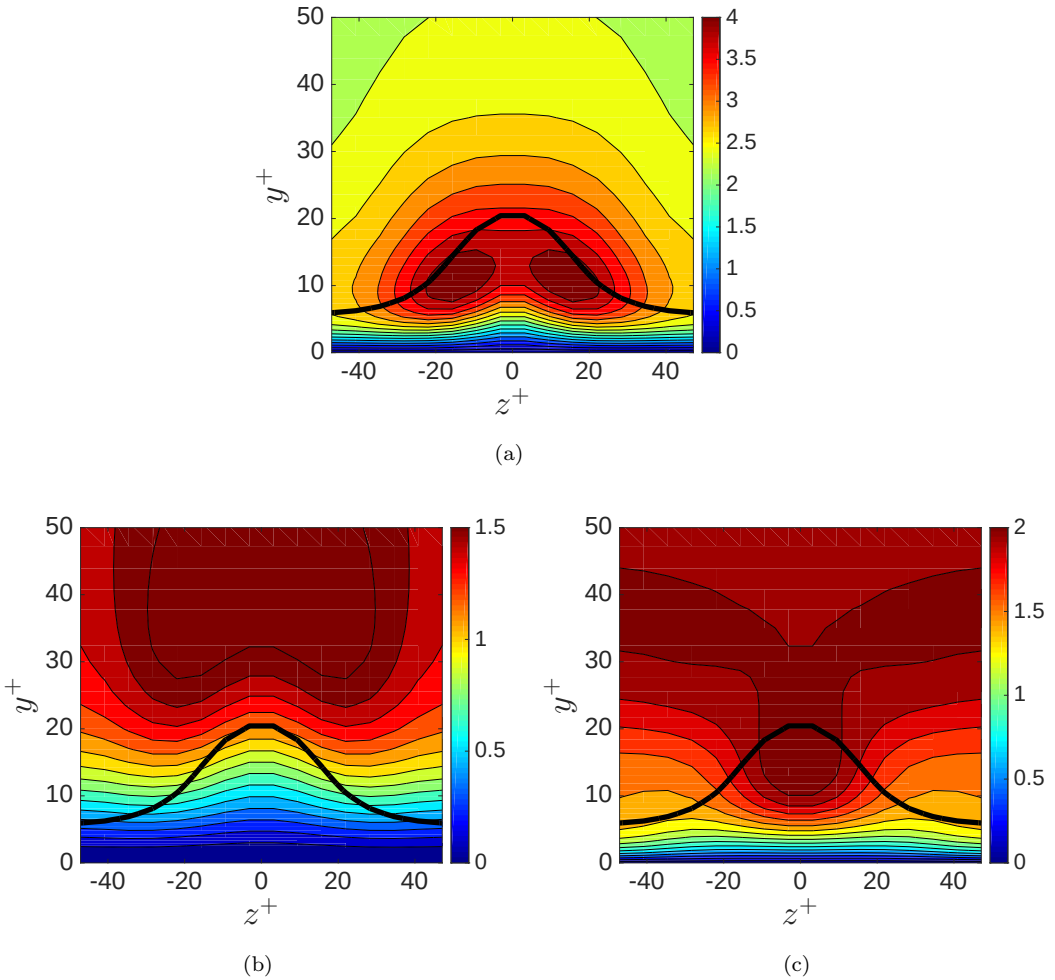

Figure 9. Velocity fluctuations around the streaky mean flow($\|\mathbf{f}\| = 2.82u_\tau^2/h$): (a) $u_{rms}(y,z)$; (b) $v_{rms}(y,z)$; (c) $w_{rms}(y,z)$. Here, the black curve indicates $U^+(y,z) = c^+$ where $c^+ = 11.76$ is the phase speed of the most energetic DMD mode (with $r = 30$, $N = 2000$).

Finally, the velocity fluctuations around the streaky mean flow $U(y,z)$ are investigated, as shown in figure 9. The regions of maximum streamwise velocity fluctuations are approximately located on the flanks of the low-speed streaks ($y \simeq 10$ and $z \pm 15 - 20$ in figure 9*a*). On the other hand, the region of the intense wall-normal velocity fluctuation is found much further from the wall ($y^+ \simeq 40 - 50$), consistent with the spectra in figure 5(*d*). Finally, the spanwise velocity fluctuation appears at the crest of the low speed streaks, and, unlike the streamwise and wall-normal velocity fluctuations, it shows the single maximum at this location. The structural features of the velocity fluctuations in the y-z plane are very similar to those of the sinuous mode of the streak instability [e.g. 22, 23, 35], directly supporting the DMD result in figure 8.

In figure 9, the velocity fluctuations are plotted with the curve $U^+(y,z) = c^+$ where c^+ is the phase speed of the most energetic DMD mode. The curve $U^+(y,z) = c^+$ is supposed to indicate the critical layer in a linear inviscid stability analysis around the streaky mean flow if the resulting eigenmode exhibits the phase speed c^+. Despite the presence of some uncertainty in the phase speed computed with DMD (the computed c^+ from the DMD is typically in the range of $8 < c^+ < 16$; figure 7*b*), the streamwise velocity fluctuations appear to be reasonably well aligned with $U^+(y,z) = c^+$. We note that the equation for the inviscid

stability analysis is supposed to be singular along $U^+(y,z) = c^+$ [39] and that the streamwise velocity component of the eigenmode of the streak instability in a laminar boundary layer was previously shown to be aligned along $U^+(y,z) = c^+$ [35]. This important similarity to the streak instability in a laminar flow suggests that the turbulent dissipation mechanism in the near-wall region does not significantly affect the inviscid inflectional mechanism of the streak instability. This issue will be further discussed in section 4.

4. Discussion

4.1. *The streamwise size of near-wall coherent structures*

Thus far, a body forcing designed to drive the streamwise uniform near-wall streaks has been implemented in a numerical experiment of a turbulent channel flow. The instantaneous velocity field and the cross-streamwise first-order statistics (section 3.1) clearly confirm that the amplified streaks are generated by the body forcing. As the forcing amplitude is gradually increased, the amplified streaks begin to generate an energetic flow structure mainly composed of the cross-streamwise velocity components. The spectra of both the wall-normal and spanwise velocities showed that the dominant streamwise wavelength of this structure is $\lambda_x^+ \approx 200 - 300$ and its wall-normal location is given at $y^+ \approx 50$. The streamwise length scale and the main wall-normal location of the structure clearly well correspond to the near-wall quasi-streamwise vortices [4]. It should be stressed that the implemented body forcing is independent of the streamwise direction. Therefore, the short streamwise wavelength observed at $\lambda_x^+ \approx 200-300$ in the spectra of the wall-normal and spanwise velocities would not be able to directly originate from the forcing itself. This suggests that the vortical structures with a finite streamwise extent are generated due to streak breakdown and the following nonlinear regeneration phase. Indeed, the streamwise wavelength of $\lambda_x^+ \approx 200-300$ agrees very well with the most unstable streamwise wavelength of the near-wall streaks in previous theoretical analysis without incorporation of background turbulence [19]. The present numerical analysis demonstrates that their analysis would be qualitatively correct even in highly turbulent flow environment. Finally, the wall-normal and spanwise velocity spectra indicate that the streamwise size of this streamwise vortical structure is bounded roughly at $\lambda_x^+ \approx 2000 - 3000$, suggesting that that the feeding mechanism of the streamwise vortices may not be possible for $\lambda_x^+ > O(1000)$. This probably explains why the streamwise length of the near-wall streaks is only $\lambda_x^+ \simeq 1000$, even though its amplification mechanism would prefer infinitely long streamwise length ($\lambda_x^+ = \infty$) according to linear theories [e.g. 14–17].

4.2. *Physical mechanism and critical layer*

Application of the DMD and further inspection of the second-order cross-streamwise statistics suggests that the amplified vortical structure at $\lambda_x^+ \approx 200 - 300$ appears to be closely associated with the 'sinuous mode' streak instability given in the form of a streamwise meandering streak and alternating cross-streamwise velocity components. The sinuous mode, which emerges in instability of streaky or streamwise vortical flows, has been well understood to originate from high spanwise mean shear in the streaky base flow: i.e. $\partial U(y,z)/\partial z$ [e.g. 22, 23, 35, 40]. The sinuous instability mode is essentially an inviscid mechanism caused by the spanwise inflection point in $U(y,z)$.

In the present study, the structure of the sinuous mode has been found to be

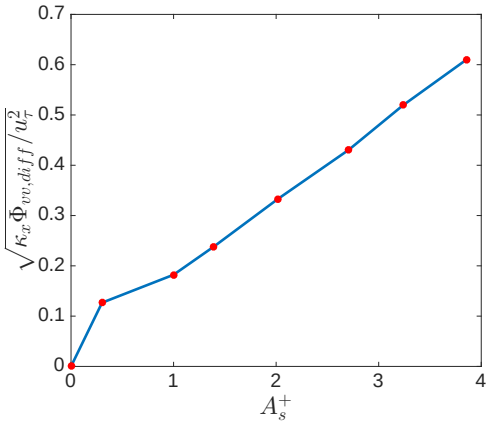

Figure 10. Amplification of the streamwise wavenumber spectrum of the wall-normal velocity ($\lambda_x^+ = 200$ and $y^+ \simeq 50$ from figure 5*b*) with the streak amplitude.

reasonably well aligned along the layer satisfying $U^+(y,z) = c^+$ (i.e. critical layer). As mentioned, in linear stability analysis around a streaky base flow, the equation of motion becomes singular in the inviscid limit with the layer satisfying $U^+(y,z) = c^+$ (i.e. the critical layer) [39], and the streamwise velocity of the instability mode has been found to be well aligned along the critical layer in the previous analysis for a laminar boundary layer [35]. Although the instability mode in the present numerical experiment does not appear to compactly reside along the critical layer as that in the inviscid stability analysis, the alignment of the streamwise velocity of the instability structure suggests that background turbulence does not significantly modify the role of the critical layer. In this respect, it is finally worth mentioning that, in the near-wall region, the inertial and dissipation length scales are not separated: indeed, both are $\delta_\nu (\equiv \nu/u_\tau)$. This implies that the role of turbulent dissipation in the near-wall region appears to be minor and that the dissipation mechanism in the near-wall region should be dominated by the molecular viscosity. This explains why the structure of the instability in relation to the critical layer remains very similar to that in a laminar flow.

4.3. *Emergence of the streak instability mode in noisy turbulent environment*

The nature of the streak instability has been understood to be subcritical, involving a strong transient growth around the streaky base flow with the sinuous mode [19, 20]. This implies that the relevant linearised system for the streak instability would be highly non-normal, resulting in strong response of the instability mode to external noise even for small streak amplitude [41]. Therefore, it is expected to be difficult to find any critical point of the emergence of instability, and this is indeed demonstrated by figure 10: the streamwise wavenumber spectrum intensity of the wall-normal velocity at $\lambda_x^+ = 200$ and $y^+ \simeq 50$ (from figure 5*b*) exhibits a rather simple monotonic growth on increasing the streak amplitude. This suggests that the growing sinuous mode instability in a streak would emerge almost immediately with the streak amplification in turbulent flow. Therefore, in practice, distinguishing streak transient growth from streak instability would be practically impossible in a turbulent flow, as was pointed out by [20].

Table A1. Energy (%) contained in $r = 30$ and $r = 50$ modes with several total numbers of modes. $N = 1000$, $\Delta t = 0.1$, $\lambda_x^+ = 200$, $\|f\| = 2.82u_\tau^2/h$.

N	30	50	70	100	120	150	180
30 modes	100	96.15	95.36	95.18	95.17	95.17	95.17
50 modes		100	99.17	98.99	98.98	98.98	98.98

5. Concluding remarks

In the present study, the emergence of near-wall streak instability has been confirmed in a fully-developed turbulent flow. The numerical experiment in this study has unambiguously demonstrated its crucial role in the generation of near-wall streamwise vortices (figure 5) as well as the selection of the streamwise length scale in the near-wall region. The present study can be extended particularly to the coherent structures in the logarithmic and outer regions emerging in the form of Townsend's attached eddies, as it was recently demonstrated that these structures also manifest the self-sustaining process in exactly the same way as in the near-wall region [24, 33]. We currently hope that this investigation plays an illuminating role in the current debate on the generation mechanism of the vortex packet in the logarithmic and outer regions: i.e. merger and growth of near-wall hairpin vortices [42] vs the streamwise vortex packet generation via streak instability [24].

Acknowledgement

This paper is dedicated to the celebration of 70th birthday of Prof. Javier Jiménez. Especially, the last author of this paper (Y.H) has been privileged with productive scientific communication with Javier over a number of years, and gratefully acknowledges this. This work is supported by Engineering and Physical Sciences Research Council (EPSRC) in the UK (EP/N019342/1).

Appendix A. Choice of parameters for Dynamic Mode Decomposition

Three main parameters of the algorithm can be combined in a large number of possibilities: number of modes r for the decomposition, and number of snapshots N and time step Δt for the data provided to the algorithm.

A.1. *The number of POD modes r*

The number of POD modes is decided based on how much energy is contained by first r POD modes. This test is performed with $N \leqslant 1000$, $\Delta t = 0.1$, $\lambda_x^+ = 200$ and $\|\mathbf{f}\| = 2.82u_\tau^2/h$, and its result is summarised for $r = 30$ and $r = 50$ in table A1. It is found that the first 30 most energetic POD modes cover approximately 95% of the total energy, and the first 50 most energetic modes cover about 99% of the energy (table A1). This result depends very little on N, for $N > 100$. In the present study, both $r = 30$ and $r = 50$ have been used.

A.2. *The number of snapshots N*

The minimum number of snapshots required is determined as follows. First, the N-th snapshot is assumed to be written as a linear combination of all the previous

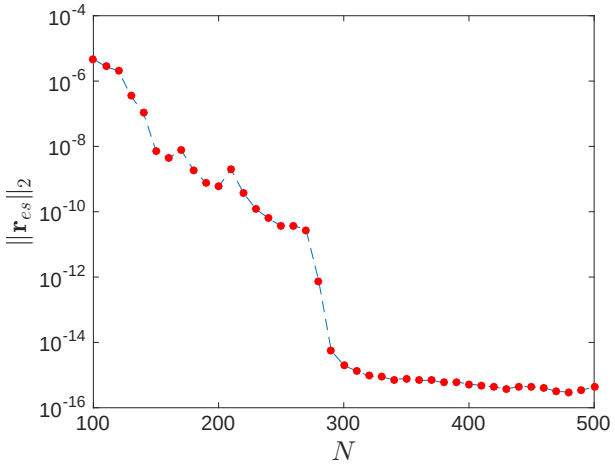

Figure A1. $\|\mathbf{r}_{es}\|_2(\equiv \sqrt{\mathbf{r}_{es}^H \mathbf{r}_{es}})$ for $r = 30$, $\lambda_x^+ = 200$, $\|\mathbf{f}\| = 2.820 u_\tau^2/h$.

$N-1$ snapshots with a residual vector $\mathbf{r}_{es}$ [25]: i.e.

$$\boldsymbol{\psi}_N = \boldsymbol{\Psi_0}\mathbf{a} + \mathbf{r}_{es}, \tag{A1}$$

where $\mathbf{a} = [a_1 \ a_2 \ ...a_{N-1}]^T$ is a column vector for the coefficients of the linear combination. We note that if the norm of $\mathbf{r}_{es}$ goes to zero for a sufficiently large N, the number of snapshots is large enough to create a subspace covering any flow field generated by a numerical simulation or an experiment. The minimum residual $\mathbf{r}_{es}$ is computed by introducing the economy-size QR decomposition of the snapshots $\boldsymbol{\Psi_0} = \mathbf{QR}$, and the coefficients of the linear combination are given by

$$\mathbf{a} = \mathbf{R}^{-1}\mathbf{Q}^H \boldsymbol{\psi}_N. \tag{A2}$$

Then, (A1) and (A2) allow us to find the residual and its norm.

Figure A1 shows the behaviour of the residual norm $\|\mathbf{r}_{es}\|_2(\equiv \sqrt{\mathbf{r}_{es}^H \mathbf{r}_{es}})$ upon increasing N. It appears that $N = 150$ is enough to represent the evolution of the flow field, as the residual norm becomes $\mathcal{O}(10^{-9})$. Above $N = 300$, the value of the residual is at $\mathcal{O}(10^{-15})$. Therefore, $N = 150$ is selected as the minimum acceptable number of snapshots. Further analysis also reveals that considering $N \approx 1000$ ensures the eigenvalues of $\mathbf{F}$ to be located along the unit circle with good precision (see figure 7*a*). For this reason, $N \geq 1000$ is considered throughout the present study.

A.3. *Snapshot time interval* Δt

Through careful inspection, the snapshot time interval for DMD has been chosen as $\Delta t^+ = 0.77$. We note that the near-wall eddy turn-over scale T^+ is at $O(10-100)$, and this value of Δt^+ was found to ensure that the eigenvalues of $\mathbf{F}$ are be located along the unit circle with good precision (see figure 7*a*). Indeed, an order-of-magnitude increase of Δt from this value has been found to yield a non-negligible random scattering of the eigenvalues of $\mathbf{F}$ along the circumference of the unit circle $|\mu| = 1$, due to low sampling frequency.

References

[1] S.J. Kline, W.C. Reynolds, F.A. Schraub, and P.W. Runstadler, *The structure of turbulent boundary layers*, Journal of Fluid Mechanics 30 (1967), pp. 741–773.
[2] C.R. Smith, and S.P. Metzler, *The characteristics of low- speed streaks in the near- wall region of a turbulent boundary layer*, Journal of Fluid Mechanics; J.Fluid Mech. 129 (1983), pp. 27–54.
[3] J. Kim, P. Moin, and R. Moser, *Turbulence statistics in fully developed channel flow at low Reynolds number*, Journal of Fluid Mechanics 177 (1987), pp. 133–66.
[4] J. Jeong, F. Hussain, W. Schoppa, and J. Kim, *Coherent structures near the wall in a turbulent channel flow*, Journal of Fluid Mechanics 332 (1997), pp. 185–214.
[5] S.K. Robinson, *Coherent motions in the turbulent boundary layer*, Annual Review of Fluid Mechanics 23 (1991), pp. 601–639.
[6] J. Jimenez, and P. Moin, *The minimal flow unit in near-wall turbulence*, Journal of Fluid Mechanics 225 (1991), pp. 213–40.
[7] J.M. Hamilton, J. Kim, and F. Waleffe, *Regeneration mechanisms of near-wall turbulence structures*, Journal of Fluid Mechanics 287 (1995), pp. 317–48.
[8] J. Jimenez, and A. Pinelli, *Autonomous cycle of near-wall turbulence*, Journal of Fluid Mechanics 389 (1999), pp. 335–359.
[9] Y. Hwang, *Near-wall turbulent fluctuations in the absence of wide outer motions*, Journal of Fluid Mechanics 723 (2013), pp. 264–88.
[10] M.T. Landahl, *Wave breakdown and turbulence*, SIAM Journal on Applied Mathematics 28 (1975), pp. 735–56.
[11] M.T. Landahl, *A note on an algebraic instability of inviscid parallel shear flows*, Journal of Fluid Mechanics 98 (1980), pp. 243–51.
[12] K.M. Butler, and B.F. Farrell, *Optimal perturbations and streak spacing in wall-bounded turbulent shear flow*, Physics of Fluids A (Fluid Dynamics) 5 (1993), pp. 774–7.
[13] S.I. Chernyshenko, and M.F. Baig, *The mechanism of streak formation in near-wall turbulence*, Journal of Fluid Mechanics 544 (2005), pp. 99–131.
[14] J.C. del Alamo, and J. Jimenez, *Linear energy amplification in turbulent channels*, Journal of Fluid Mechanics 559 (2006), pp. 205–213.
[15] G. Pujals, M. Garcia-Villalba, C. Cossu, and S. Depardon, *A note on optimal transient growth in turbulent channel flows*, Physics of Fluids 21 (2009), p. 015109 (6 pp.).
[16] Y. Hwang, and C. Cossu, *Linear non-normal energy amplification of harmonic and stochastic forcing in the turbulent channel flow*, Journal of Fluid Mechanics 664 (2010), pp. 51–73.
[17] A.P. Willis, Y. Hwang, and C. Cossu, *Optimally amplified large-scale streaks and drag reduction in turbulent pipe flow*, Physical Review E (Statistical, Nonlinear, and Soft Matter Physics) 82 (2010), p. 036321 (11 pp.).
[18] Y. Hwang, *Mesolayer of attached eddies in turbulent channel flow*, Physical Review Fluids 1 (2016), p. 064401 (18 pp.).
[19] W. Schoppa, and F. Hussain, *Coherent structure generation in near-wall turbulence*, Journal of Fluid Mechanics 453 (2002), pp. 57–108.
[20] J. Hepffner, L. Brandt, and D.S. Henningson, *Transient growth on boundary layer streaks*, Journal of Fluid Mechanics 537 (2005), pp. 91–100.
[21] J. Jimenez, J.C.D. Alamo, and O. Flores, *The large-scale dynamics of near-wall turbulence*, Journal of Fluid Mechanics 505 (2004), pp. 179–99.
[22] J. Park, Y. Hwang, and C. Cossu, *On the stability of large-scale streaks in turbulent Couette and Poiseulle flows*, Comptes Rendus de l'Academie des Sciences Serie II b/Mecanique 339 (2011), pp. 1–5.
[23] F. Alizard, *Linear stability of optimal streaks in the log-layer of turbulent channel flows*, Physics of Fluids 27 (2015), p. 105103 (20 pp.).
[24] Y. Hwang, *Statistical structure of self-sustaining attached eddies in turbulent channel flow*, Journal of Fluid Mechanics 767 (2015), pp. 254–289.
[25] P.J. Schmid, *Dynamic mode decomposition of numerical and experimental data*, Journal of Fluid Mechanics 656 (2010), pp. 5–28.
[26] M.R. Jovanovic, P.J. Schmid, and J.W. Nichols, *Sparsity-promoting dynamic mode decomposition*, Physics of Fluids 26 (2014).
[27] W.C. Reynolds, and A.K.M.F. Hussain, *The mechanics of an organized wave in turbulent shear flow. III. Theoretical models and comparisons with experiments*, Journal of Fluid Mechanics 54 (1972), pp. 263–88.
[28] P. Moin *Fundamentals of engineering numerical analysis*, Cambridge University Press, Cambridge, 2001.
[29] P.J. Schmid *Stability and transition in shear flows*, Softcover reprint of the original First 2001 Springer, New York, 2001.
[30] F. Waleffe, *Homotopy of exact coherent structures in plane shear flows*, Physics of Fluids 15 (2003), pp. 1517–1534.
[31] T.R. Bewley *Numerical Renaissance: Simulation, Optimization, and Control*, Reinassance Press, 2014.
[32] J. Kim, and P. Moin, *Application of a fractional-step method to incompressible Navier-Stokes equations*, Journal of Computational Physics 59 (1985), pp. 308–23.
[33] Y. Hwang, and Y. Bengana, *Self-sustaining process of minimal attached eddies in turbulent channel flow*, Journal of Fluid Mechanics 795 (2016), pp. 708–38.
[34] M. de Giovanetti, Y. Hwang, and H. Choi, *Skin-friction generation by attached eddies in turbulent channel flow*, Journal of Fluid Mechanics 808 (2016), pp. 511–538.
[35] P. Andersson, L. Brandt, A. Bottaro, and D.S. Henningson, *On the breakdown of boundary layer streaks*, Journal of Fluid Mechanics 428 (2001), pp. 29–60.

[36] M. Marquillie, U. Ehrenstein, and J.P. Laval, *Instability of streaks in wall turbulence with adverse pressure gradient*, Journal of Fluid Mechanics 681 (2011), pp. 205–240.
[37] A. Zare, M.R. Jovanovic, and T.T. Georgiou, *Color of turbulence*, (2016).
[38] J. Kim, and F. Hussain, *Propagation velocity of perturbations in turbulent channel flow*, Physics of Fluids A (Fluid Dynamics) 5 (1993), pp. 695–706.
[39] P. Hall, and N.J. Horseman, *Linear inviscid secondary instability of longitudinal vortex structures in boundary layers*, Journal of Fluid Mechanics 232 (1991), pp. 357–375.
[40] D.S. Park, and P. Huerre, *Primary and secondary instabilities of the asymptotic suction boundary layer on a curved plate*, Journal of Fluid Mechanics 283 (1995), pp. 249–272.
[41] P.J. Schmid, *Nonmodal stability theory*, Annual Review of Fluid Mechanics 39 (2007), pp. 129–162.
[42] R.J. Adrian, *Hairpin vortex organization in wall turbulence*, Physics of Fluids 19 (2007), pp. 41301–1.